Direct ink writing of 3D thermoelectric architectures for fabrication of micro power generators

Fredrick Kim
Ulsan National Institute of Science and Technology (UNIST)
Seong Eun Yang
Ulsan National Institute of Science and Technology (UNIST)
Hyejin Ju
Ulsan National Institute of Science and Technology (UNIST)
Seungjun Choo
Ulsan National Institute of Science and Technology (UNIST)
Jungsoo Lee
Ulsan National Institute of Science and Technology (UNIST)
Gyeonghun Kim
Ulsan National Institute of Science and Technology (UNIST)
Soo-Ho Jung
Korea Institute of Materials Science
Suntae Kim
Ulsan National Institute of Science and Technology (UNIST)
Chaenyung Cha
Ulsan National Institute of Science and Technology (UNIST)
Kyung Tae Kim
Korea Institute of Materials Science (KIMS)
Sangjoon Ahn
Ulsan National Institute of Science and Technology (UNIST)
Han Gi Chae
Ulsan National Institute of Science and Technology (UNIST)
Jae Sung Son (jsson@unist.ac.kr)
Ulsan National Institute of Science and Technology (UNIST)

Article

Keywords: 3D thermoelectric architectures, micro-thermoelectric modules

Posted Date: February 4th, 2021

DOI: https://doi.org/10.21203/rs.3.rs-146528/v1

Version of Record: A version of this preprint was published at Nature Electronics on August 9th, 2021. See the published version at https://doi.org/10.1038/s41928-021-00622-9.

Abstract

Micro-thermoelectric modules can be used to develop unique components such as energy harvesters, active coolers, and thermal sensors in various integrated systems. However, the manufacturing of these modules still relies on costly traditional micro-fabrication processes, producing only two-dimensional (2D) thermoelectric films. This limitation severely constrains temperature gradient formation across thermoelectric films, and hence, the sufficient amount of power required to run integrated systems is not generated. Herein, we present the direct ink writing of micro-scale three-dimensional (3D) thermoelectric architectures for fabricating high-performance micro-thermoelectric generators. The characteristics of $(Bi, Sb)_2(Te, Se)_3$-based particles were precisely engineered such that the colloidal inks achieved outstanding viscoelasticity, thereby facilitating the creation of complex 3D architectures having high thermoelectric figure-of-merits of 1.1 (p-type) and 0.5 (n-type). Micro-thermoelectric generators made of 3D-written vertical filaments exhibited large temperature gradients and a good resulting power density, opening an avenue for the cost-effective and rapid manufacturing of integrated micro-thermoelectric modules.

Main Text

Micro-thermoelectric (μ-TE) modules have been regarded as potential electronic components that can generate power from minimal heat flow or act as coolers for local heat management [1,2]. Depending on the dimensions of the TE legs, μ-TE modules can be easily integrated into various emerging systems such as Internet of things–based devices, wearable electronic devices, wireless sensor networks, and lab-on-a-chip devices[3-5]. Most of these systems are expected to be energy autonomous because they are usually embedded in enclosed environments or packaged within inaccessible structures[5-7]. In this context, μ-TE modules can provide a unique solution for ensuring sustainable electricity supply owing to their advantages of a simple device structure, high reliability and durability, and maintenance-free operation. Moreover, μ-TE device arrays can potentially be used in applications involving high-resolution infrared image sensors, gas sensors, and thermal imaging sensors[8].

Advancements in micro-electromechanical system (MEMS) technology have facilitated the design and fabrication of micro-scale integrated systems consisting of multiple functional units of electrical and mechanical components[9]. This micro-fabrication process based on traditional lithography, deposition, etching, and release also allows us to create patterned, planar two-dimensional (2D) TE legs and electrodes in a μ-TE module with a thickness of tens of micrometres[10,11]. However, the mass fabrication techniques used in MEMS technology have the potential problem of costly multi-step complicated processes, which rely on expensive lithography equipment. More importantly, these 2D design processes are not suitable for the fabrication of structural three-dimensional (3D) TE legs with high aspect ratios in a μ-TE module; this 3D nature is especially critical in creating a large temperature gradient across a TE leg and obtaining high power in a μ-TE generator (μ-TEG)[12,13]. The bulk micro-machining MEMS technique has been used to make 3D structures, but the approach is limited in terms of materials, scale, and complexity and has a high cost and long processing time[9,14].

The recent advancement in 3D printing technology has revolutionised the design and manufacturing of any arbitrary complex 3D structure[15,16]. Despite considerable progress in recent years, materials that can be used to print on a micrometre or nanometre scale are still mostly limited to photo-curable resins or their composites with inorganics, and printing is carried out by stereolithographic techniques[17]. Alternatively, the extrusion-based direct writing process of colloid inks containing inorganic particles or precursors has attracted great interest because of its simplicity in processing, affordable equipment price, and a wider range of printable materials[18,19]. In this process, it is of paramount importance to optimise the viscoelastic properties of the applicable functional inks in a highly specific range, in order to maintain structural integrity during printing and the functionality of the printed object[20,21]. The most conventional strategy of adding organic binders to secure viscoelasticity often leads to critical degradation of electrical or mechanical functionality of inorganic printed objects, especially TE materials, due to lowered sintering efficiency[22-25]. Recently, several approaches have been reported to fabricate TE modules by 3D printing of Bi_2Te_3, BiSbTe, SnSe, and skutterudites-based TE legs[22-27]. For example, inorganic ionic binders have been used to achieve moderate viscoelasticity in colloid inks and thereby realise the layer-wise deposition of 3D TE structures without degradation of TE performance[28,29]. However, the 3D printed TE structures developed thus far suffer from critically low resolution due to limited printability of inks and diminished functionality of the printed materials. Therefore, in order to seamlessly integrate into various microscale systems, it is imperative to attain high-resolution 3D printing of TE materials and modules.

In this study, we realised the 3D direct ink writing of $(Bi, Sb)_2(Te, Se)_3$-based p- and n-type inks to build arbitrarily shaped 3D TE architectures with high aspect ratios toward the fabrication of high-power μ-TEGs (Fig. 1a). $(Bi, Sb)_2(Te, Se)_3$-based alloys are regarded as the best TE materials for operations at temperatures less than 100 °C [30-34], making them the most suitable candidates for power generation from low-grade heat dissipated from integrated systems. We precisely engineered various characteristics of the TE particles, such as overall size, size distribution, and surface charge states to achieve an extremely high viscoelasticity of the TE inks without using organic rheological modifiers. Based on this rheological design of inks, we demonstrated the direct 3D writing of the inks to print 3D filaments in a dimension-controlled manner, fabricating highly performant 3D TE architectures such as arches and lattices standing on a substrate by computer-aided model (CAD)-based design. To show the feasibility of the current direct writing process, we fabricated μ-TEGs chipped with the direct written 3D TE legs on a substrate and characterised their power performance, thereby demonstrating that the proposed process is the most cost-effective and rapid method of manufacturing high-performance μ-TE modules.

3D direct ink writing of TE materials

The system used for the extrusion-based 3D direct ink writing of TE materials (Fig. 1a) consists of a nozzle connected to a syringe containing viscoelastic TE ink, which is extruded by a pneumatic pressure controller that is moved in the *x*, *y*, and *z* axis according to a CAD-based pre-design. Considering the rheological properties of the inks and the TE properties of the sintered materials, p-type $Bi_{0.55}Sb_{1.45}Te_3$ with a $Sb_2Te_4^{2-}$-based chalcogenidometallate (ChaM) content of 25 wt% and n-type $Bi_2Te_{2.7}Se_{0.3}$ with a

ChaM content of 10 wt% were chosen for 3D-printing experiments. The detailed rheological and TE properties are discussed in the following sections. Standing TE filaments were vertically printed on a Si/SiO_2 substrate (Supplementary Videos 1). The filaments exhibited excellent structural retention with smooth lateral surfaces in a single pass. Moreover, various printing parameters such as the dispensing pressure and nozzle diameter were controlled, and thereby, the diameters of TE filaments were precisely controlled from 180 μm to 810 μm at the sintered states (Fig. 1b and 1c). This shows the diverse applicability of the current process in multiple scales ranging from micrometres to millimetres. Optical microscopic (OM) images (Fig. 1f) revealed that the written filaments with various diameters had the uniform line widths with a standard deviation less than 10 μm (Supplementary Fig. 1). Moreover, the maximum aspect ratios achieved by the written filaments reached 4.9–9.4, depending on the diameter (Fig. 1d and 1e). This capability to print highly anisotropic 3D TE filaments by direct writing made it possible to build complex 3D architectures. As an example, Fig. 1g presents an arched architecture consisting of junctional p- and n-type TE legs fabricated by the direct writing process, where the uniformity in line width is not significantly changed at bent filaments or junctions. Moreover, a 3D lattice was built by the layer-by-layer deposition of TE filaments (Fig. 1h and 1i, Supplementary Video 2). At the junctions, individual filaments maintained their primary architectures without merging or thickening, which demonstrates the structural retention of the inks (Fig. 1j). These examples of complex 3D structures indicate the potential of using the proposed process to fabricate p-n junctions in 3D patterned TE semiconductors and 3D porous TE structures for controlled thermal transport.

When the as-printed structures were heat treated, the TE particles in the 3D structures were well consolidated by the sintering promotion effect of the ChaM additives, leading to the formation of effectively sintered grains in the microstructure and robust 3D structures at the macroscale[28]. The OM and scanning electron microscopy (SEM) images of the sintered filaments in the printed 3D lattice (Fig. 1k and 1l) revealed that the TE filaments maintained their primary architecture. Moreover, the TE filaments at the junction were well fused together without crack formation (Fig. 1m). The high-resolution SEM images of p- and n-type TE filaments (Supplementary Fig. 2) showed grain sizes of several tenths of micrometres, which further indicated that the grain growth was effective. Although significant volume shrinkage is unavoidable in 3D-printed structures, high reproducibility was obtained for all the samples in all directions. Typically, the volume contracted by 36% during sintering at 450 °C for 30 min; these sintering conditions are required to obtain a competitive TE performance of materials. Thus, we could design the final 3D architecture according to the CAD-based pre-design.

Ink design and rheological properties

Controlling the viscoelastic properties of inks is of paramount importance for securing reliable flow through fine nozzles and ensuring the structural integrity of the printed filament. Our group previously demonstrated that the addition of ChaM inorganic ions provides the required viscoelasticity to TE-particle-containing colloidal inks, thereby facilitating the shape-conformable 3D printing of TE materials by layer-wise ink deposition[28]. However, the direct writing of TE inks without organic binders requires considerable improvement in the rheological properties to achieve smooth and reliable extrusion and

faster structural recovery after printing. Hence, we attempted to optimally design the ink viscoelasticity by controlling the size, size distribution, and surface states of TE particles. Fig. 2a shows a schematic description of the strategy used in the current study: control of the TE particle (1) size and (2) size distribution, and (3) surface oxidation of particles to obtain a stable ink system using ChaM.

Fig. 2b and 2c, and Supplementary Fig. 3 show the particle size distribution with a median particle size and the effect of the distribution on the dynamic viscosities (η') of the corresponding TE particle colloids, respectively. A smaller average particle size and narrower particle size distribution produced a higher η' in inks because the effective volume of a smaller particle system was greater. A wider distribution in the particle size may lead to aggregation, which can result in clogging during printing[35-39]. Accordingly, the shear stress dependencies of the storage (G') and loss (G") moduli of colloidal inks (Supplementary Fig. 4) were measured to evaluate the linear viscoelasticity region and phase stability, respectively. The smallest TE particle system (D_{median}=4.378 μm) exhibited higher critical stress value (30.8 Pa) than those of the larger particle systems (D_{median}=8.759 μm and 17.276 μm; 4.2 and 1.5 Pa, respectively), indicating the ability to sustain higher shear stress without losing the structural integrity of the ink. In addition, higher G" after critical stress may also suggest that the former system possesses superior phase stability as compared to those of latter cases[40]. It should be noted that regardless of particle size, the colloidal inks all demonstrated higher G' than G" at a wide range of shear stress, indicating their highly viscous semisolid behaviour (Supplementary Fig. 4).

Our previous research showed that the addition of ChaM is unavoidable for obtaining high-quality TE devices by sintering, where voids are filled and the particles are structurally transformed from molecular ions to the crystalline phase[28]. In the present study, we found that as-synthesised non-oxidised TE particles have weak negative surface charges (Fig. 2d). The inks composed of these non-oxidised TE particles are inherently unstable even in the presence of the counter ions of ethylenediammonium in the ChaM anions, which may screen the electrostatic surface charge on the TE particles ('screen effect') and induce irreversible aggregation[41]. To overcome this problem, controlled surface oxidation and the incorporation of ChaMs were carried out to investigate their effect on the viscoelasticities of various inks. The degree of oxidation of the TE particles was investigated by ζ-potential measurement, Fourier transform infrared (FTIR) spectroscopy, and X-ray photoelectron spectroscopy (XPS) (Fig. 2d and 2e, Supplementary Figs. 5 and 6). In both p- and n-type, the X-ray diffraction (XRD) patterns of the oxidised particles were identical to those of the non-oxidised ones, suggesting that the oxidised surface layers were very thin or amorphic (Supplementary Fig. 7). However, the FTIR spectra of the oxidised particles clearly showed a peak indexed to OH stretching, which indicated surface oxidation, and this observation was further supported by the XPS spectra, which showed oxide peaks. More importantly, the surface charges of TE particles became neutral by the oxidation, minimizing the screen effect caused by the ChaM additives (Fig. 2d). Consequently, the viscoelastic properties of the oxidised TE particles containing ChaM showed dramatic enhancement in various rheological properties, whereas those of the non-oxidised TE particles containing ChaM worsened owing to the screening effect. The quality of the ChaM-containing inks was assessed by the rheological properties: (1) shear stress dependency of G' (Fig. 2f,

Supplementary Fig. 8), (2) dynamic viscosity in the static state (Fig. 2g, Supplementary Fig. 8), (3) initial slope of the increase in G' as a function of the shear rate (Fig. 2h, top), and (4) yield stress (Fig. 2h, bottom). In addition, the structure recovery of inks after deposition is one of the most critical factors to ensure shape retention. To evaluate the structure recovery, three interval thixotropy tests (3ITTs) were comparatively performed for the oxidised and non-oxidised particle-based inks with the 25 wt% ChaM content (Fig 2i). 3ITTs are designed to measure the rate and degree of elastic recovery (G') after inducing structural disruption via increasing shear stress. It is very important to note that the oxidised TE particle-based ink exhibited reduced structure disruption upon high shear stress and immediate elastic recovery, as compared to those of the non-oxidised particle ink, suggesting the strong inter-particle interaction. These intriguing results confirmed that the surface oxidation coupled with ChaM significantly improved the 3D printability, by attaining both shear thinning and fast elastic recovery that are rarely demonstrated for extremely high viscous fluids, especially for those without organic binders. This combination of attractive viscoelastic properties is expected to realise a highly-desired field of binder-free, all-inorganic inks for precise direct writing process.

TE properties of direct-written 3D structures

The remarkable sinterability observed in direct-written TE filaments was clearly reflected in their excellent TE properties. The XRD spectra of both p- and n-type particles showed patterns corresponding to bulk $Bi_{0.5}Sb_{1.5}Te_3$ and $Bi_2Te_{2.7}Se_{0.3}$ with slight peak shifts, indicating the effective sintering of materials into a single phase (Fig. 3a). We varied the ChaM content for both p-type $Bi_{0.55}Sb_{1.45}Te_3$ and n-type $Bi_2Te_{2.7}Se_{0.3}$ particles, and the highest figure-of-merit (*ZT*) values were observed for 25% and 10% ChaM content for the p- and n-type particles, respectively (Supplementary Fig. 11). Accordingly, the characterisations and the related discussion were described for the corresponding samples. The room-temperature electrical conductivities and Seebeck coefficients of the direct-written TE filaments were 607.7 S m^{-1} and 191.13 μV K^{-1} (p type) and 793.1 S m^{-1} and 111.7 μV K^{-1} (n type), respectively (Fig. 3b and 3c), which are comparable to the reported values for $(Bi, Sb)_2(Te,Se)_3$-based bulk alloys with corresponding compositions. Simultaneously, we comparatively characterised the TE properties of 3D-printed p- and n-type TE bulk cuboids that were 12.7 mm wide and 1.0–2.0 mm thick and found that their electrical conductivities and Seebeck coefficients were identical to those of the TE filaments within the measurement error range (10%). Thus, the homogeneous TE properties of the 3D-printed samples were independent of their dimensions, which demonstrated the expansibility of the current process to materials ranging from micrometre-scale single filaments to centimetre-scale 3D bulks obtained by fusing layer-wisely deposited TE filaments without the loss of TE performance.

The temperature dependence of TE properties at 300–525 K was characterised using 3D-printed TE bulk cuboids because of the difficulty involved in measuring a micro-scale single filament. The electrical conductivities of the p- and n-type samples decreased with increasing temperatures, indicating the degenerate behaviour of semiconductors. Moreover, the Seebeck coefficients of both the samples generally increased with increasing temperatures. The Seebeck coefficient of the p-type samples was

196.6 μV K^{-1} at room temperature with a peak value of 216.3 μV K^{-1} at 423 K, whereas that of the n-type samples was 110.1–132.0 μV K^{-1} over the entire measured temperature range (Fig. 3d). The p- and n-type samples had carrier mobilities of 197.6 and 81.7 cm^2 V^{-1} s^{-1}, respectively, characterised by the Hall effect measurement. These high carrier mobilities are comparable to the reported values of $(Bi, Sb)_2(Te, Se)_3$-based bulk alloys with corresponding compositions and are responsible for the high electrical conductivity of the 3D printed samples[33,42]. The carrier concentrations of the p- and n-type samples were 2.1 10^{19} and 6.3 10^{19} cm^{-3}, respectively. Since the Seebeck coefficient is reciprocally proportional to the carrier concentration, the relatively low Seebeck coefficient of the n-type sample compared with the corresponding bulk values is attributed to the high carrier concentration[33]. Thus, the p- and n-type samples had high TE power factors of 2.6 and 1.0 mW m^{-1} K^{-2}, respectively, at 300 K (Supplementary Fig. 12).

The temperature-dependent thermal conductivity of the p-type and n-type samples was 0.74–1.15 W m^{-1} K^{-1} over the entire measured temperature range (Fig. 3e), which was significantly reduced in comparison to 1.5–2.5 W m^{-1} K^{-1} of bulk Bi_2Te_3-based materials[42]. This reduction in the thermal conductivities is attributed to phonon scattering at the pore sites of the printed TE materials, which had relative densities of 82% and 72% for the p- and n-type samples, respectively. Because the as-printed samples were sintered under pressure-less conditions without pre-compaction, 20%–30% porosity was unavoidable. These macroscale pores are beneficial for enhancing the *ZT* values by the reduction of the thermal conductivity. For example, Lidorenko et al. theoretically predicted an increase of 30% in the ratio of electrical conductivity to thermal conductivity for porous SiGe alloys[43]. Moreover, there have been several reported instances of experimental evidence for the enhanced *ZT* values of porous TE materials[44-47]. The thermal properties of the 3D-printed samples are further discussed in the Supplementary Information (Supplementary Fig. 13).

These promising electrical and thermal properties led to markedly high *ZT* values for the p- and n-type 3D-printed samples. The p- and n-type 3D-printed samples had *ZT* values of 0.92 and 0.37, respectively, at room temperature (Fig. 3f). Furthermore, the maximum *ZT* values of 1.03 and 0.50 were achieved at 350 and 420 K for the p- and n-type TE materials, respectively. These values are comparable to those obtained for typical Bi_2Te_3 and BiSbTe ingots ($ZT \approx 0.8–1.0$)[48], and enhanced from the reported value of 0.9 for the 3D printed BiSbTe materials[28]. To the best of our knowledge, the *ZT* values reported in this paper are one of the highest for TE materials produced from TE inks or pastes[22-24,27].

Fabrication and power measurement of μ-TEG

When combined with traditional patterning processes, our ink writing technique can facilitate the heterogeneous integration of TE legs into patterned electrode arrays, thereby making it possible to fabricate μ-TEGs in a rapid, direct, and cost-effective manner. Moreover, the shape engineerability of the current process makes it possible to design TE legs for optimised thermal transfer, maximising the temperature gradient and resulting output power of μ-TEGs. We fabricated a μ-TEG composed of 3D-

printed vertical TE filaments with a diameter of 350 μm and a height of 1400 μm. The TE leg thickness of the fabricated μ-TEG is at least an order of magnitude greater than that of previously reported μ-TEGs prepared by the traditional MEMS, hot-pressing and dicing, and screen-printing processes[1,6,10,49,50]. Moreover, the p- and n-type TE legs were directly printed on a Si/SiO_2 substrate using pre-patterned Ag electrodes (width: 500 μm), which were fabricated by screen printing with a shadow mask (Fig. 4a and 4b, and Supplementary Video 3). The printed TE legs were electrically connected using Ag adhesive. The top of the module was further covered with a water-captured hydrogel cooler for maintaining a temperature difference between the hot and cold sides. Polyacrylamide hydrogel, with a high amount of strongly bound water within the polymeric matrix, prevented premature water evaporation and allowed the sustained maintenance of water-cooling capability at a wide range of temperature.

The module resistance was 92 Ω at room temperature. Upon heating, the hot-side temperature gradually increased from room temperature to 121.8 °C, whereas the cold-side temperature remained at less than 48 °C (Supplementary Fig. 14). Accordingly, the temperature difference across the μ-TEG increased up to 82.9 °C, which is an order of magnitude higher than the typical temperature gradient observed in previously reported μ-TEGs upon heating[6,11,50]. The creation of such a high temperature difference in the current system is attributed to the high aspect ratio of the 3D-printed TE legs. As the temperature difference increased, the output voltage increased almost linearly and the output power increased quadratically (Fig. 4c and 4d), achieving a maximum output voltage of 42.4 mV and a power of 2.8 μW at a temperature difference of 82.9 °C. Moreover, the maximum power density reached 479.0 μW cm^{-2}, which is sufficient to run advanced wireless sensor networks[3-5,7,51]. These results clearly demonstrate the practicability of 3D direct writing for manufacturing high-performance μ-TEGs that can be integrated into electronic systems.

Conclusions

This study demonstrated direct ink writing using highly viscoelastic TE inks for designing micro-scale geometries of 3D TE materials and power generators. By optimising the particle size, size distribution, and surface states of ink materials, we developed all-inorganic TE inks with extremely high viscoelasticity, which is suitable for 3D direct writing. This particle design strategy can be extended to diverse classes of functional materials to synthesise 3D-printable inks without using organic rheological modifiers, which could facilitate the conservation of the primary properties of particles in 3D-printed structures, as indicated by the high ZT values obtained for direct-written TE filaments. When combined with traditional lithographic processes, our direct writing approach can facilitate the integration of μ-TE modules into various emerging electronic systems, in which the modules can function as power generators for energy-autonomous systems or as Peltier coolers for heat management. We consider the proposed approach to be an important step toward achieving a broad technological adaption of 3D-printable materials in electronic device manufacturing.

Methods

Materials

Granules of Bi, Sb, Te and Se (99.999%) were purchased from 5N Plus. Ethanethiol (>97%), ethylenediamine (>99.5%), acetonitrile (>99.8%) and glycerol (>99.5%), were purchased from Aldrich. All elements and chemicals were used without further purification.

Synthesis of $(Bi, Sb)_2(Te, Se)_3$-based TE particles

TE powders with the stoichiometric composition of $Bi_{0.55}Sb_{1.45}Te_3$ and $Bi_2Te_{2.7}Se_{0.3}$ were prepared by mechanical alloying (MA) process. For the synthesis of $Bi_{0.55}Sb_{1.45}Te_3$ particles with the D_{median} of 4.378 µm, zirconia grinding balls with the diameter of 5 mm were loaded into 80 mL of a zirconia milling jar and the weight ratio of ball-to-powder was fixed at 5:1(Fritsch Monomill, Pulverisette, Germany). The rotation speed of the planetary mill was 450 rpm and the time of alloying process was for 11 h. The particles with the D_{median} of 17.276 µm were synthesised under the same conditions in 240 ml of a zirconia milling jar. The particles with the D_{median} of 8.759 µm were synthesised by mechanical alloying using SPEX Mill (8000M Mixer-Mill, SPEX) with stainless steel balls including two balls (φ = 12.7 mm) and four balls (φ = 6.35 mm) for 5 h. In all samples, agglomerated particles were removed by sieving the particles to < 45 µm.

Synthesis of all-inorganic $(Bi, Sb)_2(Te, Se)_3$-based ink

The Sb_2Te_4 ChaM was synthesised by dissolving 0.32 g of Sb powder and 0.64 g of Te powder in a co-solvent of 2 ml of ethanethiol and 8 ml of ethylenediamine at room temperature in a N_2–filled glove box. The Sb_2Te_4 solution was stirred for over 24 h until the particles fully dissolved to produce a dark purple colour. Anti-solvent of acetonitrile was added to the solution with the volume ratio of 8:1, which is followed by centrifugation at 6615 g for 10 min to precipitate out the precursor. The precipitate was dried under vacuum for 30 minutes to produce Sb_2Te_4 ChaM powder. A mixture of 4 g of the TE powder and desired amount of the ChaM were dispersed in 4 g of glycerol, and the solution was mixed with a planetary centrifugal mixer (ARM-100, Thinky) for 2 h to fully homogenise the ink.

Rheological properties of the ink

The rheological properties of TE inks were measured using a rotational rheometer (Haake MARS III, Thermo Scientific) equipped with a coaxial cylinder geometry at 25 °C. The stress sweep tests were conducted over the range of 0.005 – 300 Pa at a frequency of 1 rad s^{-1} and the frequency sweep tests were carried out before and after stress sweep test at a constant stress of 1 Pa to assess the phase stability of ink. The three-interval thixotropy tests (3ITTs) at various stresses also conducted as reported elsewhere[40]. The 1st interval was conducted under constant shear stress of 0.1 Pa (linear viscoelastic range) for 120 s, the 2nd interval was done at various stresses (1, 5, 10, 50, and 200 Pa) for 120 s. The 3rd interval was attempted at a shear stress of 0.1 Pa for 300 s in order to evaluate the structural recovery of ink after deposition during 3D printing.

Direct 3D writing process

Direct writing was executed using an in-house pneumatic extrusion-based 3D printer with a nozzle connected to an ink reservoir, a pressure controller, a compressor unit and a three-axis stage with a stepper motor. Ink was loaded in a 5 ml syringe barrel (Saejong) with a metal needle of inner diameters ranging from 80 to 310 μm and deposited in a z-axis at 0.25 mm s^{-1}. The pressure control unit was adjusted to extrude a high aspect ratio filament.

Materials characterisation

XRD patterns were collected by using X'pert Pro (PANalytical) with a Cu Kα X-ray source (wavelength of 1.5418 nm), operating at 40 kV and 30 mA equipped with an X'Celerator detector. The microstructure was characterised by using a field-effect SEM (Nova-NanoSEM230, FEI and S-4800, Hitachi High-Technologies) operated at 10 kV. The optical microscopic images were obtained using an Olympus BX51M. The CCD images were obtained by a CCD camera (MicroPublisher 5.0 RTV, QImaging). Particle size distributions of the TE powders were determined with Laser particle size analyser (LS13 320, Beckman Coulter). ζ-potential of the particles was determined by a Zetasizer (Nano ZS, Malvern). The surface functional groups of the particles were obtained using a FT-IR spectrometer (Varian 670/620) in attenuated total reflectance (ATR) mode over the scanning range of 650-4000 cm^{-1}. XPS measurements were performed by an X-ray photoelectron spectrometer (K-alpha, Thermo Scientific).

TE properties of 3D-printed samples

The room-temperature electrical conductivity of the filaments was measured using the sheet resistance of the samples by a four-point method (Keithley 2400 multimeter controlled Lab trace 2.0 software, Keithley Instrument, Inc.) The room-temperature Seebeck coefficienct was obtained by using home-built set-up where the temperature gradient and the open circuit voltage were measured using a Keithley 2400 source-meter. Seebeck coefficient was calculated by the slope of the measured voltages versus the applied temperature differences ranging from 1 K to 15 K, which was measured by two T-type thermocouples.

The temperature-dependent electrical conductivity and the Seebeck coefficients of the bulk materials were measured simultaneously under Ar atmosphere in the temperature range from 300 K to 525 K using thermal analyzer (SBA458 Nemesis, Netzsch, Germany). A typical sample for measurement had cuboid shape with the dimension of 10×10×2 mm^3. The thermal conductivity (κ) was calculated from the relationship $\kappa = \rho C_p D$, where ρ is the density, C_p is the specific heat capacity and D is the thermal diffusivity. The thermal diffusivity was measured in the temperature range 300 K to 525 K by using laser flash analyzer (LFA-457, Netzsch, Germany). The specific heat capacity was determined using the rule of mixtures with the previously reported specific heat capacity values of Bi_2Te_3 and Sb_2Te_3[52,53]. The density was estimated by measuring the volume and weight of the cuboid shape. The carrier concentrations and mobilities were measured at room temperature by using a Hall measurement system (HMS-8400, Lake Shore) with the magnetic field of 10T.

Fabrication and output power characterization of the μ-TEG

Ag electrodes were screen-printed on a SiO_2 wafer using Ag-containing adhesive (Pyro-Duct 597-A, Aremco, USA) as illustrated in Supplementary Fig. 15. On top of the Ag electrodes, 3 pairs of n-type and p-type TE filaments were extruded out of a metal needle with the inner diameter of 210 μm. The printed filaments were initially dried at 110 °C on a hot plate for 5 minutes, and annealed at 450 °C for 30 minutes in a tube furnace flowing a gas mixture of 15% H_2 and 85% Ar. Each pair of TE filaments was electrically connected in series and thermally in parallel by bridging Ag-containing adhesive on top of the annealed filaments. To measure the temperature difference across each pair of TE filaments, two T-type thermocouples were attached to the surface of the SiO_2 wafer (hot side) and on top of the Ag electrodes (cold side). The ceramic heater (10 mm×10 mm) was used as a heat source and the cold side temperature was maintained below 48^{o}C by attaching polyacrylamide (PAAm) hydrogel on top of the μ-TEG. The PAAm hydrogel was separately fabricated by radical polymerisation of 10 % (w/v) acrylamide and 0.5 % (w/v) N,N'-methylenebisacrylamide, with 0.2 % (w/v) ammonium persulfate and 0.2 % (w/v) N,N,N',N'-tetramethylethylenediamine as co-initiators[54]. For the measurement of power generation, the TEG was connected to a Keithley 2400 at each temperature differences and the maximum power output (P) was calculated using $P=V^2/4R$. Thermal silicone grease (YYTG-201, Youngyiel) was applied between the heater, and μ-TEG to minimise thermal contact resistance.

Declarations

Data availability

The data that support the plots within this paper and other findings of this study are available from the corresponding author upon reasonable request.

Acknowledgments

This work was supported by Samsung Research Funding Center of Samsung Electronics under Project No. SRFC-MA1801-05

Author Contributions

F.K., S.E.Y., H.J., H.G.C., and J.S.S. designed the experiments, analysed the data and wrote the paper. F.K., S.E.Y., S.C., J.L., J.S. and K.K.T. carried out the synthesis and basic characterisation of the materials. S.E.Y., H.J., and H.G.C. performed the characterisation of rheological properties. F.K., S.E.Y., G.K. and S.A. performed the characterisation of thermoelectric properties. F.K. and S.E.Y. carried out the fabrication and measurement of TEGs. S.K. and C.C. performed the synthesis of hydrogels. All authors discussed the results and commented on the manuscript.

Additional information

Supplementary Information is available for this paper. Reprints and permissions information is available at www.nature.com/reprints. Correspondence and requests for materials should be addressed to J.S.S.

Competing financial interests

The authors declare no competing financial interests.

References

1 Haras, M. & Skotnicki, T. Thermoelectricity for IoT – A review. *Nano Energy* **54**, 461-476 (2018).

2 Ando J. et al. A review of the development and applications of thermoelectric microgenerators for energy harvesting. *Renew. Sustain. Energy Rev.* **91**, 376-393 (2018).

3 Pletcher, N. M. et al. A 52 μW wake-up receiver with -72 dBm sensitivity using an uncertain-IF architecture. *IEEE J. Solid-State Circuits* **44**, 269-280, (2009).

4 Gilbert, J. M. & Balouchi, F. Comparison of energy harvesting systems for wireless sensor networks. *Inter. J. Autom. Comput.* **5**, 334-347 (2008).

5 Zhang, Y. et al. A Batteryless 19 μW MICS/ISM-Band energy harvesting body sensor node SoC for ExG applications. *IEEE J. Solid-State Circuits* **48**, 199-213 (2013).

6 Yan, J. et al. Review of micro thermoelectric generator. *J. Microelectromech. Syst.* **27**, 1-18 (2018).

7 Rabaey, J. M. et al. PicoRadios for wireless sensor networks: The next challenge in ultra-low power design. *IEEE ISSCC Digest of Technical Papers*, 200-201 (2002).

8 Park, S. C. et al. A micro-thermoelectric gas sensor for detection of hydrogen and atomic oxygen. *Analyst* **134**, 236-242 (2009).

9 Blachowicz, T. & Ehrmann, A. 3D printed MEMS technology-recent developments and applications. *Micromachines (Basel)* **11,** (2020).

10 Dhawan, R. et al. $Si_{0.97}Ge_{0.03}$ microelectronic thermoelectric generators with high power and voltage densities. *Nat. Commun.* **11**, 4362 (2020).

11 Li, G. et al. Integrated microthermoelectric coolers with rapid response time and high device reliability. *Nat. Electron.* **1**, 555-561 (2018).

12 Hong, C. T. et al. Spray-printed CNT/P3HT organic thermoelectric films and power generators. *J. Mater. Chem. A.* **3**, 21428-21433 (2015).

13 Wang, Y. et al. Flexible thermoelectric materials and generators: challenges and innovations. *Adv. Mater.* **31**, 29 (2019).

14 Mehran, M. & Zorman, C. SiC MEMS opportunities and challenges for applications in harsh environments. *Thin Solid Films.* **355-356**, 518-524 (1999).

15 Davidson, E. C. et al. 3D printable and reconfigurable liquid crystal elastomers with light-induced shape memory via dynamic bond exchange. *Adv. Mater.* **32**, 1(2020).

16 Hensleigh, R. et al. Charge-programmed three-dimensional printing for multi-material electronic devices. *Nat. Electron.* **3**, 216-224 (2020).

17 Vyatskikh, A. et al. Additive manufacturing of 3D nano-architected metals. *Nat. Commun.* **9**, 593 (2018).

18 Lewis, J. A. & Ahn, B. Y. Device fabrication: Three-dimensional printed electronics. *Nature* **518**, 42-43 (2015).

19 Sun, K. et al. 3D printing of interdigitated Li-ion microbattery architectures. *Adv. Mater.* **25**, 4539-4543 (2013).

20 Lewis, J. A. Direct ink writing of 3D functional materials. *Adv. Funct. Mater.* **16**, 2193-2204 (2006).

21 Jo, S. et al. Ink Processing for Thermoelectric Materials and Power-Generating Devices. *Adv. Mater.* **31**, 20 (2019).

22 Zhang, B. et al. Promising thermoelectric properties of commercial PEDOT:PSS materials and their Bi_2Te_3 powder composites. *ACS Appl. Mater. Interfaces* **2**, 3170-3178 (2010).

23 Kato, K. et al. Fabrication of bismuth telluride thermoelectric films containing conductive polymers using a printing method. *J. Electron. Mater.* **42**, 1313-1318 (2013).

24 Ou, C. et al. Fully Printed Organic-Inorganic nanocomposites for flexible thermoelectric applications. *ACS Appl. Mater. Interfaces* **10**, 19580-19587 (2018).

25 He, M. et al. Thermopower enhancement in conducting polymer nanocomposites via carrier energy scattering at the organic–inorganic semiconductor interface. *Energy Environ. Sci.* **5,** (2012).

26 Burton, M. R. et al. 3D Printed SnSe thermoelectric generators with high figure of merit. *Adv. Energy Mater.* **9,** (2019).

27 Su, N. et al. 3D-printing of shape-controllable thermoelectric devices with enhanced output performance. *Energy* **195,** (2020).

28 Kim, F. et al. 3D printing of shape-conformable thermoelectric materials using all-inorganic Bi_2Te_3-based inks. *Nat. Energy* **3**, 301-309 (2018).

29 Yang, S. E. et al. Composition-segmented BiSbTe thermoelectric generator fabricated by multimaterial 3D printing. *Nano Energy* **81,** (2021).

30 Kim, S. I. et al. Thermoelectrics. Dense dislocation arrays embedded in grain boundaries for high-performance bulk thermoelectrics. *Science* **348**, 109-114 (2015).

31 Li, J.-F. et al. High-performance nanostructured thermoelectric materials. *NPG Asia Mater.* **2**, 152-158 (2010).

32 Saeidi-Javash, M. et al. 3D Conformal printing and photonic sintering of high-performance flexible thermoelectric films using 2D nanoplates. *Adv. Funct. Mater.* **29,** (2019).

33 Snyder, G. J. & Toberer, E. S. Complex thermoelectric materials. *Nat. Mater.* **7**, 105-114 (2008).

34 Bark, H. et al. Effect of multiwalled carbon nanotubes on the thermoelectric properties of a bismuth telluride matrix. *Curr. Appl. Phys.* **13**, S111-S114 (2013).

35 Willenbacher, N. & Georgieva, K. Rheology of disperse systems. *Product Design and Eng.* 7-49 (2013).

36 Barthelmes, G. et al. Particle size distributions and viscosity of suspensions undergoing shear-induced coagulation and fragmentation. *Chem. Eng. Sci.* **58**, 2893-2902 (2003).

37 Luckham, P. F. & Ukeje, M. A. Effect of particle size distribution on the rheology of dispersed systems. *J. Colloid Interface Sci.*, **220**, 347-356 (1999).

38 Chen, Z. et al. Preparation of high solid loading and low viscosity ceramic slurries for photopolymerization-based 3D printing. *Ceram. Int.* **45**, 11549-11557 (2019).

39 Maranzano, B. J. & Wagner, N. J. The effects of interparticle interactions and particle size on reversible shear thickening: Hard-sphere colloidal dispersions. *J. Rheol.* **45**, 1205-1222 (2001).

40 Eom, Y. et al. Rheological design of 3D printable all-inorganic inks using BiSbTe-based thermoelectric materials. *J. Rheol.* **63**, 291-304 (2019).

41 Hong, B. J. et al. Successful stabilization of graphene oxide in electrolyte solutions: enhancement of biofunctionalization and cellular uptake. *ACS Nano*, **6**, 63-73 (2012).

42 Zheng, G. et al. High thermoelectric performance of p-BiSbTe compounds prepared by ultra-fast thermally induced reaction. *Energy & Environ. Sci.* **10**, 2638-2652 (2017).

43 Lidorenko, N.S. et al. Influence of porosity and intergrain-boundary quality on the electrical and thermal conductivities of semiconductive thermoelectric materials. *Inorg. Mater.* **6,** (1970).

44 Wu, C.-A. et al. Low thermal conductivity and enhanced zT values of porous and nanostructured $Cu_{1-x}Ni_x$ alloys. *Chem. Eng. J.* **368**, 409-416 (2019)

45 Khan, A. U. et al. Nano-micro-porous skutterudites with 100% enhancement in ZT for high performance thermoelectricity. *Nano Energy* **31**, 152-159 (2017).

46 Chang, P. H. et al. Giant thermoelectric effect in graphene-based topological insulators with heavy adatoms and nanopores. *Nano. Lett.* **14**, 3779-3784 (2014).

47 Ning, H. et al. Enhanced thermoelectric performance of porous magnesium tin silicide prepared using pressure-less spark plasma sintering. *J. Mater. Chem. A.* **3**, 17426-17432 (2015).

48 Yan, X. et al. Experimental studies on anisotropic thermoelectric properties and structures of n-type $Bi_2Te_{2.7}Se_{0.3}$. *Nano. Lett.* **10**, 3373-3378 (2010).

49 Rojas, J. P. et al. Review—Micro and nano-engineering enabled new generation of thermoelectric generator devices and applications. *ECS J. Solid State Sci. Tech.* **6**, N3036-N3044 (2017).

50 Francioso, L. et al. Flexible thermoelectric generator for ambient assisted living wearable biometric sensors. *J. Power Sources.* **196**, 3239-3243 (2011).

51 Paradiso, J. A. & Starner, T. Energy scanvenging for mobile and wireless electronics. *IEEE Pervasive Comput*. **4**, 1 (2005).

52 Pashinkin, A. S. et al. The heat capacity of solid antimony telluride Sb_2Te_3. *Russ. J. Phys. Chem. A.* **82**, 878-879 (2008).

53 Liu, W. et al. Studies on the Bi_2Te_3–Bi_2Se_3–Bi_2S_3 system for mid-temperature thermoelectric energy conversion. *Energy Environ. Sci.* **6**, 552-560 (2013).

54 Kim, M. & Cha, C. Modulation of functional pendant chains within poly(ethylene glycol) hydrogels for refined control of protein release. *Sci. Rep.* **8**, 4315 (2018).

Figures

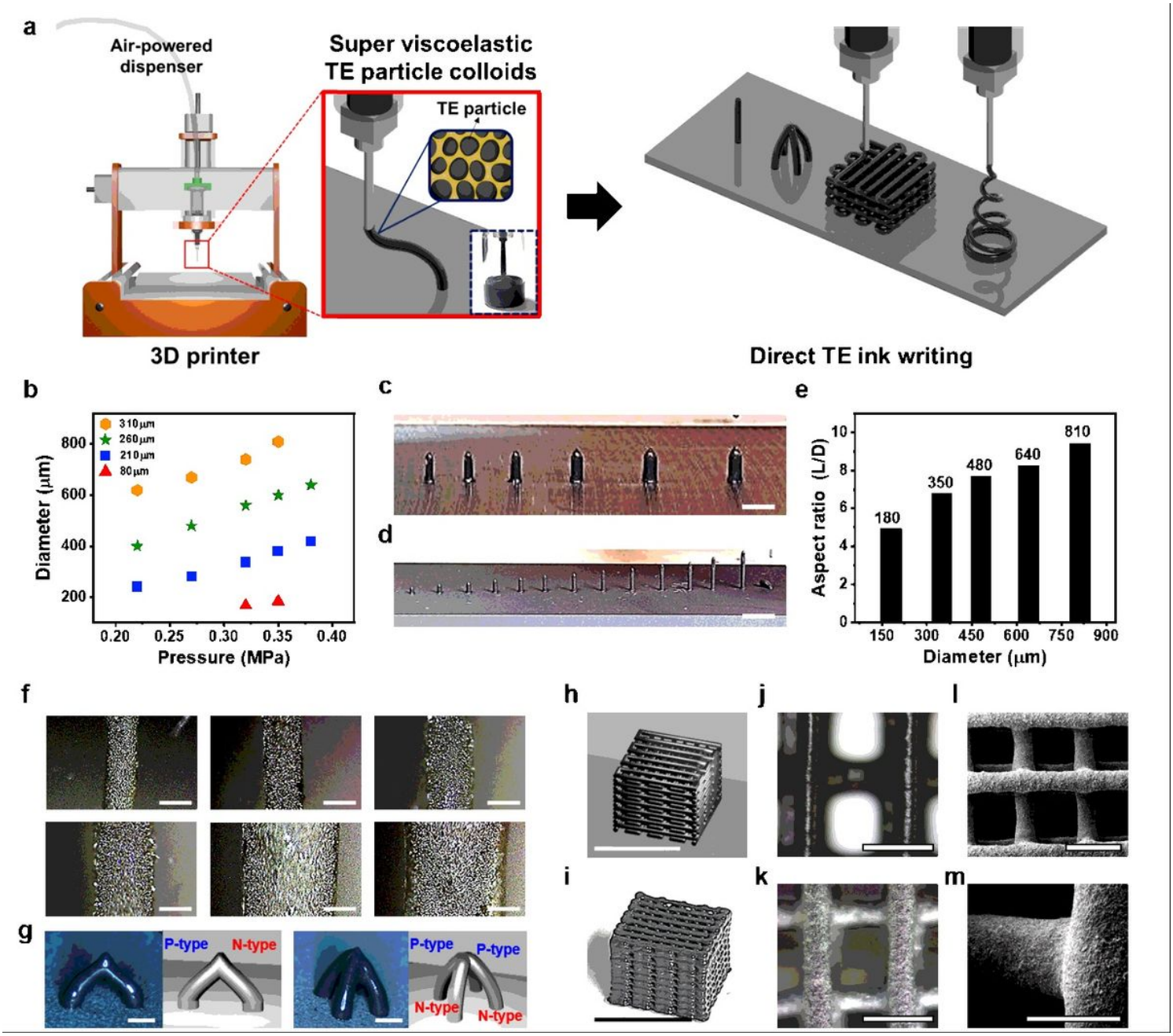

Figure 1

Direct 3D writing of TE inks. a, Schematic illustration of the direct ink writing for 3D TE architectures. b, The plot of the diameters of 3D filaments versus the dispensing pressure with different inner diameters of nozzles. c,d, Photographs showing 3D filaments with different diameters (c) and aspect ratios (d). Scale bars, 2 mm. e, Maximum aspect ratio (length/diameter) of the written TE filaments with respect to the diameters. f, OM image of TE filaments with diameters of 180, 240, 340, 420, 560, and 620 μm. Scale bars, 200 μm. g, Charge-coupled device (CCD) image and illustrated pre-models of arch-type architectures consisting of junctional p- and n-type TE legs. Scale bars, 500 μm. h,i, Illustrated model (h), and photograph (i), of the 3D lattice built by the layer-by-layer deposition of TE filaments. Scale bars, 10 mm. j,k, OM images (j) of the as-printed and (k), sintered 3D lattice. Scale bars, 500 μm. l,m, Low- (l) and high-magnification (m) SEM images of the 3D lattice. Scale bars, 500 μm.

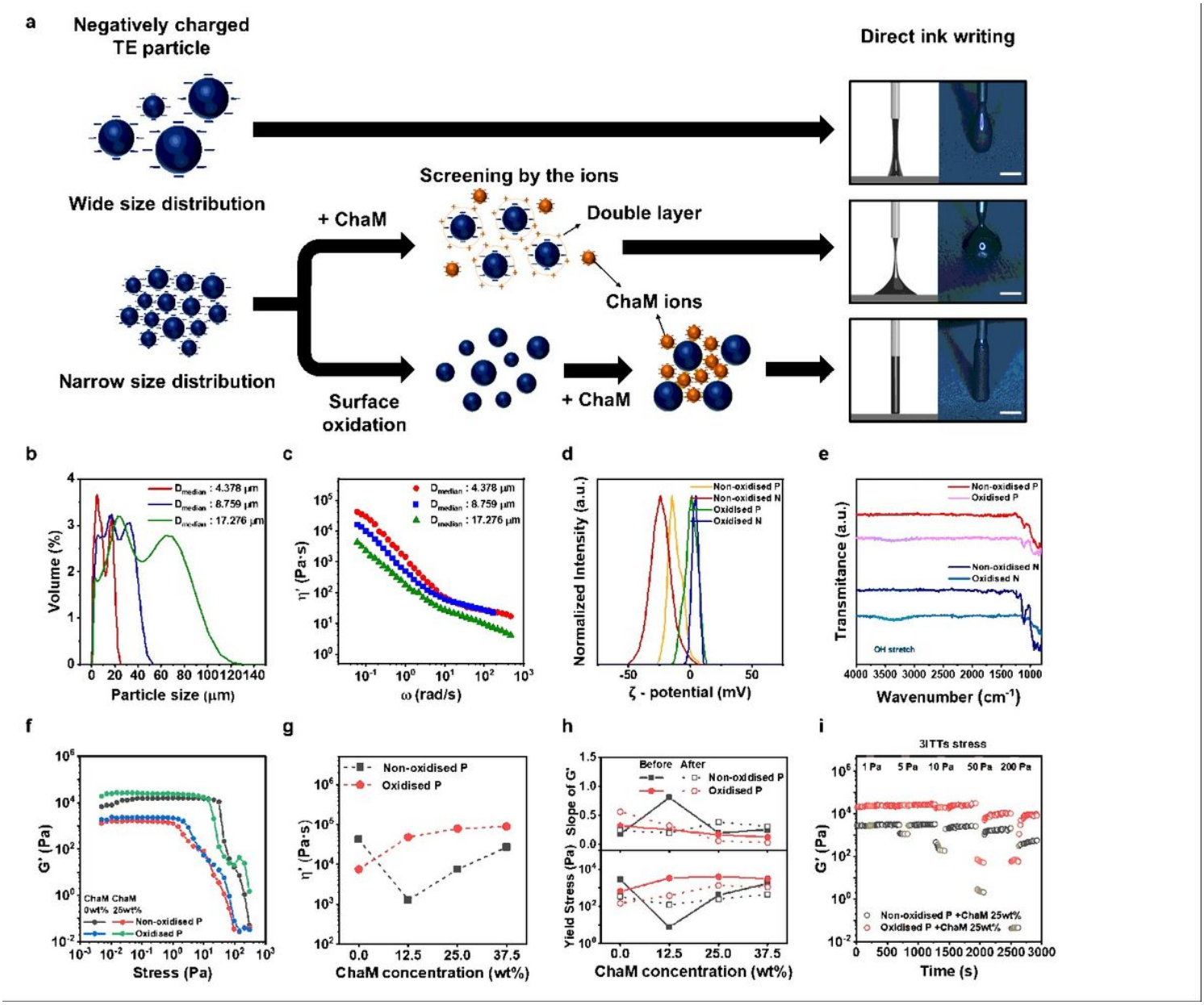

Figure 2

Rheological property of super viscoelastic TE ink. a, Scheme showing the design principle of super viscoelastic TE particle inks with respect to their size, size distribution, and surface oxidation. Scale bars, 500 μm. b,c, Particle size histograms (b) and dynamic viscosity (η') (c) of p-type Bi0.55Sb1.45Te3 TE particle inks. Dmedian denotes the median particle diameter. d,e, The ζ-potential curves (d) and FT-IR spectrum (e) of oxidised and non-oxidised p- and n-type TE particles in colloids. f, Storage modulus (G') curves of oxidised and non-oxidised p-type TE particle inks containing 0 wt% and 25 wt% ChaM obtained from the stress sweep test. Dynamic frequency sweep results of oxidised and non-oxidised p-type TE particle inks with various ChaM contents. g,h, η' values (scatter style) at static state and viscosity ratio (bar style) between η'before (η' before stress sweep) and η'after (η' after stress sweep) at 0.1 rad/s (g), and slope of the G' curve (top) and yield stress (bottom) before and after stress sweep test. (h). i, G' of the

TE inks having 25 wt% ChaM in the sequential 3ITT measurement (top) and the recovery ratio between G' after 300 s in 3rd interval (G'3) and G' at static state (G'0).

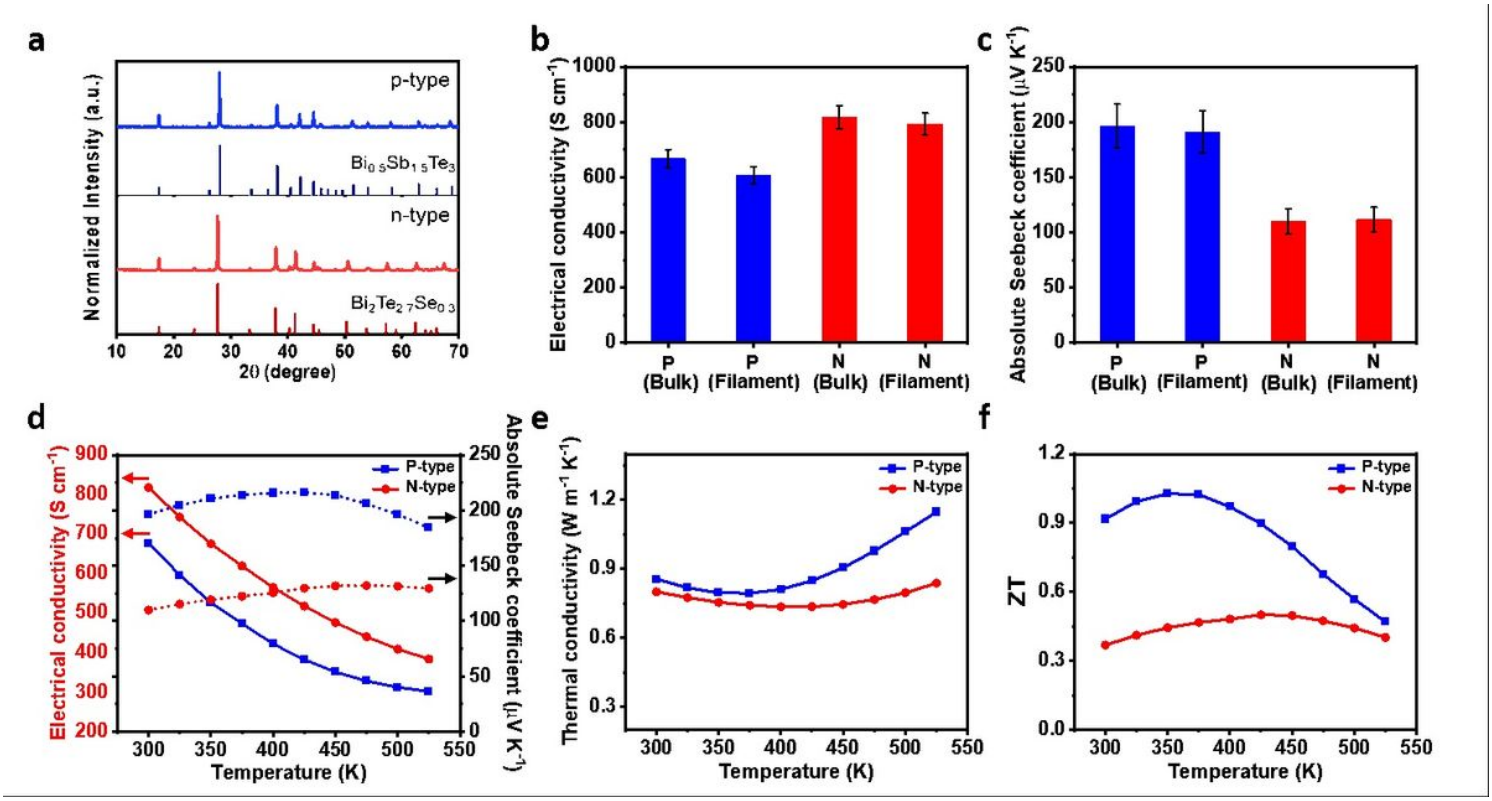

Figure 3

TE properties of the 3D-printed samples. a, XRD patterns of the 3D-printed n-type and p-type filaments. The vertical lines indicate the peaks corresponding to bulk Bi0.5Sb1.5Te3 (JCPDS: 00-049-1713) and Bi2Te2.7Se0.3 (JCPDS: 00-015-0863). b,c, Comparison of the room-temperature electrical conductivity (b) and Seebeck coefficient (c) of the p-type and n-type 3D-printed filaments and bulk cuboids. d–f, Temperature-dependent TE properties of the n-type and p-type 3D-printed samples: electrical conductivities and absolute Seebeck coefficient s (d), thermal conductivities (e) and ZT values (f).

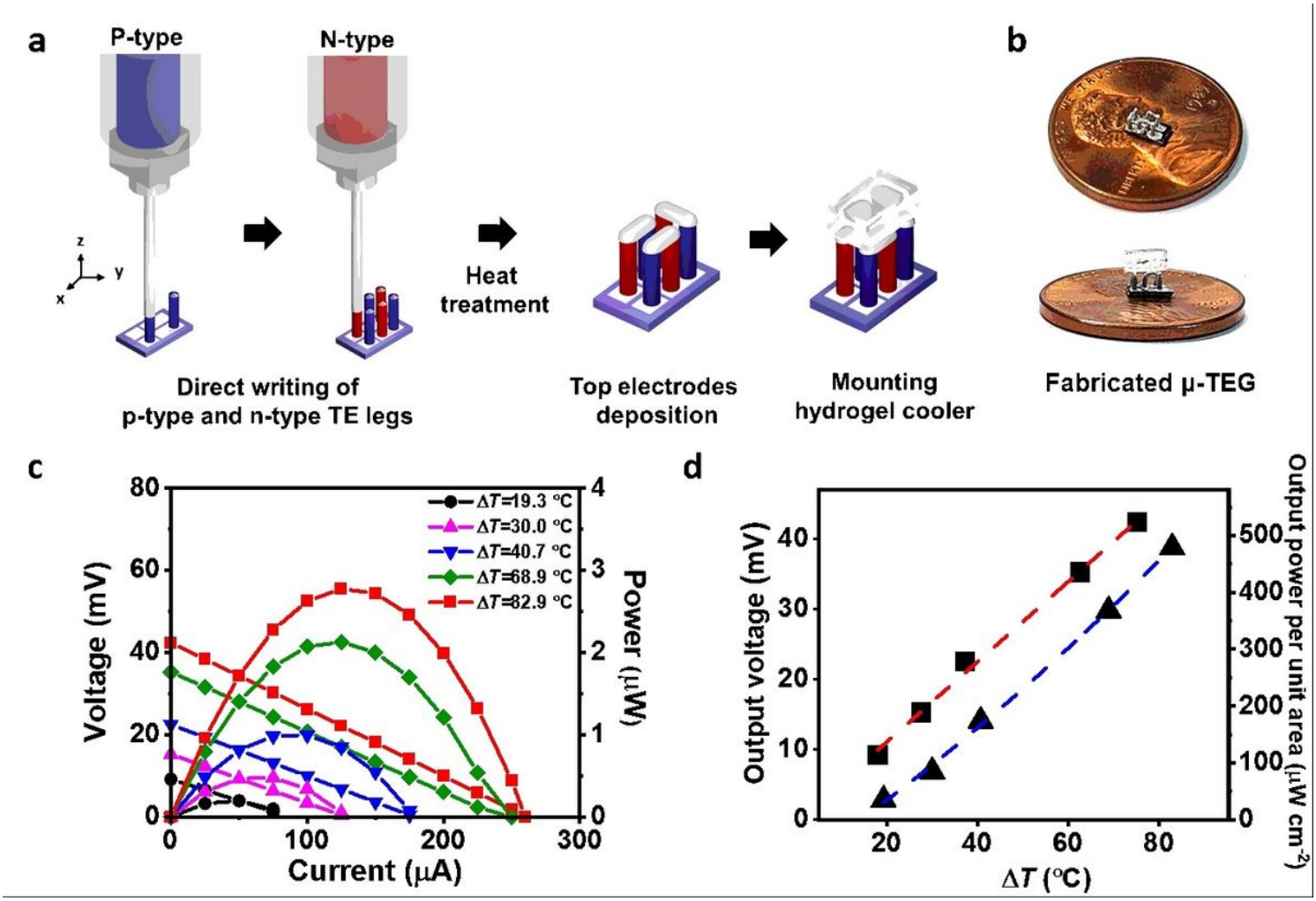

Figure 4

Fabrication and power performance of the μ-TEG. a, Schematic illustration showing the fabrication of the μ-TEG by direct 3D ink writing. b, Photograph of the fabricated μ-TEG. c, Output voltage and power of the μ-TEG at various temperature differences. d, Output voltage and power density of the μ-TEG as a function of temperature differences.

Supplementary Files

This is a list of supplementary files associated with this preprint. Click to download.

- SupplementaryVideo1.mp4
- SupplementaryVideo2.mp4
- SupplementaryVideo3.mp4
- SupplementaryInformation.pdf